Annu. Rev. Phys. Chem. 2005. 56:281–308
doi: 10.1146/annurev.physchem.56.092503.141204

VIBRATIONAL AUTOIONIZATION IN POLYATOMIC MOLECULES[1]

S.T. Pratt
Argonne National Laboratory, Argonne, Illinois 60439 USA; email: stpratt@anl.gov

Key Words molecular photoionization, nonadiabatic effects

■ **Abstract** The vibrationally autoionizing Rydberg states of small polyatomic molecules provide a fascinating laboratory in which to study fundamental nonadiabatic processes. In this review, recent results on the vibrational mode dependence of vibrational autoionization are discussed. In general, autoionization rates depend strongly on the character of the normal mode driving the process and on the electronic character of the Rydberg electron. Although quantitative calculations based on multichannel quantum defect theory are available for some polyatomic molecules, including H_3, only qualitative information exists for most molecules. This review shows how qualitative information, such as Walsh diagrams along different normal coordinates of the molecule, can provide insight into the vibrational autoionization rates.

1. INTRODUCTION

From the earliest days of molecular orbital theory, correlation diagrams for diatomic molecules have been used to show how the orbitals changed in going from separated atoms to bound molecules to united atoms (1, 2). Given the occupancy of different orbitals, such correlation diagrams made it possible to predict which states would be bound or repulsive, as well as which potential curves would have humps or other interesting features. Mulliken's early correlation diagrams (1, 2) are exceedingly detailed, as he made an effort to show not only which molecular and united-atom orbitals correlated with which separated-atom limit, but also how the orbital energies changed as a detailed function of the internuclear distance. Building on Mulliken's work, Walsh (3) published a classic series of papers in 1953 in which he used qualitative correlation diagrams to illustrate how orbital energies in polyatomic molecules depend on molecular geometry, particularly on

[1]The submitted manuscript has been created by the University of Chicago as Operator of Argonne National Laboratory ("Argonne") under Contract No. W-31-109-ENG-38 with the U.S. Department of Energy. The U.S. Government retains for itself, and others acting on its behalf, a paid-up, nonexclusive, irrevocable worldwide license in said article to reproduce, prepare derivative works, distribute copies to the public, and perform publicly and display publicly, by or on behalf of the Government.

bond angles. The Walsh diagrams that emerged from this work allow the prediction of molecular geometry as a function of orbital occupancy in a great variety of molecules, and they are still widely used today. Over the years, scientists have tried to put these diagrams on a more quantitative footing (4). Qualitative and quantitative arguments about how orbital energies change as a function of geometry or along reaction coordinates are at the heart of many popular theories of chemical reactivity (e.g., Woodward-Hoffman rules, frontier molecular orbital theory, etc.) and have seen wide applications in organic and inorganic chemistry (5–7). This review shows how studies of vibrational autoionization in small polyatomic molecules can provide information on how orbital energies change as a function of geometry near the equilibrium configuration of the molecule and how qualitative correlation diagrams can provide insight into vibrational autoionization in polyatomic molecules.

Vibrational autoionization is a form of radiationless transition in which a highly excited, quasi-bound molecule decays into the ionization continuum through the conversion of vibrational energy into electronic energy of the electron to be ejected, resulting in a free electron and an ion (8). As an illustration, Figure 1 shows an energy level diagram of H_3 and H_3^+, in which the $10\,pa_2''$, $N = 0$ Rydberg state converging to the vibrationally excited ($v_1 = 1$, $v_2^l = 0^\circ$), $N^+ = 1$, $K^+ = 0$ state of H_3^+ lies above the energy of the $H_3^+\,{}^1A_1'$ vibrationless ground state. By

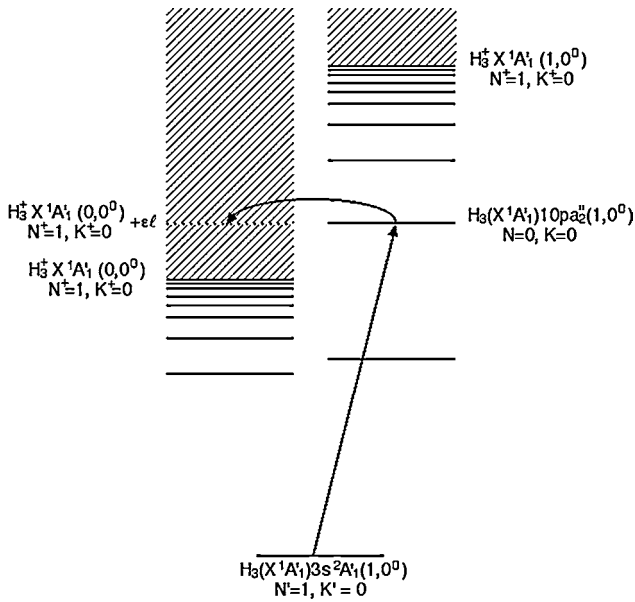

Figure 1 Schematic diagram of vibrational autoionization of the $10\,pa_2''$, $(1, 0^\circ)$, $N = 0, K = 0$ Rydberg state of H_3 via the symmetric stretch, ν_1.

converting the ν_1 quantum into electronic energy, the electron can escape into the ($v_1 = 0, v_2 = 0^\circ$) continuum. The required coupling between the vibrational and electronic degrees of freedom make vibrational autoionization an inherently nonadiabatic process, and its relative simplicity make it an attractive model for more general nonadiabatic processes. The rate of this process is expected to depend on the principal quantum number, n, the orbital angular momentum and its projection on the molecular symmetry axis, ℓ and Λ, respectively, the vibrational quantum numbers and the character of the excited normal modes, and the rotational quantum numbers of the autoionizing level. In general, double-resonance laser techniques (9, 10) can be used to prepare the autoionizing states in a state-selective manner so that the decay process can be studied as a function of these relevant quantum numbers. In addition, photoelectron spectroscopy can be used to characterize the product vibrational state distribution and, in some instances, the product rotational state distribution (11, 12). In this fashion, the autoionization mechanism can be characterized and compared with theoretical models. In this review, the emphasis is on understanding why some normal modes are efficient drivers of vibrational autoionization and why some are not, and on understanding how the process depends on the electronic symmetry of the Rydberg electron. The correlation diagrams of Mulliken and Walsh (1–3) are valuable tools for developing this understanding, which should ultimately provide insight into a much broader class of nonadiabatic processes in small polyatomic molecules.

Vibrational autoionization is perhaps best understood in the context of multichannel quantum defect theory (MQDT) (13–15). Thus, the remainder of this review begins with a discussion of some basic concepts of MQDT. Within this theory, the principal parameters that drive the autoionization process are the geometry-dependent body frame quantum defects, and these are related in a qualitative manner to the correlation diagrams and Walsh diagrams discussed above. These concepts are then illustrated with experimental results on vibrational autoionization in three small polyatomic molecules: H_3, NH_3, and NO_2. Finally, several directions for future investigations are discussed.

The experimental work described here emphasizes frequency-domain measurements using photoionization mass spectrometry and dispersive photoelectron spectroscopy. Rather than provide a comprehensive review of past work, I have focused on only a few examples; there has been significant work in this field that is not mentioned here, and there has been considerable recent progress in using time-domain techniques to study molecular autoionization processes with Rydberg wavepackets. Fortunately, the review by Fielding in the present volume (16) helps address this deficiency.

2. THEORETICAL BACKGROUND

In the first theoretical investigations of vibrational autoionization, Berry (8) directly evaluated the terms left out of the molecular Hamiltonian as a result of the Born-Oppenheimer approximation, i.e., the terms involving derivatives of the

electronic and vibrational wavefunctions with respect to the vibrational coordinates. Consideration of the general properties of these matrix elements for molecular Rydberg states led him to propose a propensity rule stating that all else being equal, the autoionization process with the minimum change in vibrational quantum numbers will dominate (8, 17–20). Thus, when energetically allowed, $\Delta v = -1$ processes are expected to be the fastest vibrational autoionization route. This prediction has received experimental confirmation in a variety of diatomic and polyatomic molecules (21–25a,b). Unfortunately, quantitative calculations based on this approach have been only moderately successful (18–20).

The development of MQDT provided a new perspective on the spectroscopy and dynamics of molecular Rydberg states, as well as a quantitative and qualitative framework in which to understand autoionization phenomena (13–15, 26, 27). In the following, approximate formulae for the vibrational autoionization rate that were derived from MQDT are presented along with a physical rationalization of their form. These are followed by a limited but more general discussion of MQDT. Readers interested in the details of MQDT and its applications are referred to a number of excellent reviews (13–15).

Herzberg & Jungen (28) made the first application of MQDT to vibrational autoionization in their study of the Rydberg states of H_2. For Rydberg states described by pure Hund's case b, they derived an expression for the autoionization width, Γ, in terms of the R-dependent quantum defect $\mu_{\ell\lambda}(R)$, where ℓ is the orbital angular momentum of the Rydberg electron and λ is its projection on the molecular axis. In the absence of ℓ mixing, this expression is

$$\Gamma_{\nu_i,\ell,\lambda,v_i,v_f} = \frac{2\pi 2\mathcal{R}}{\nu_i^3}\left[\frac{d\mu_{\ell\lambda}(R)}{dR}\right]^2_{R_e^+} |\langle\chi_{v_f}(R)|R - R_e^+|\chi_{v_i}(R)\rangle|^2, \qquad 1.$$

where $\mathcal{R}$ is the Rydberg constant, ν_i is the effective principal quantum number of the initial state, χ_v is the vibrational wavefunction of the v^{th} vibrational level of the ion, and R_e^+ is the equilibrium internuclear distance of the ion. The R-dependent quantum defect is given by the modified Rydberg formula

$$V_{\ell\lambda}(R) = V^+(R) - \frac{\mathcal{R}}{[n - \mu_{\ell\lambda}(R)]^2}, \qquad 2.$$

where $V_{\ell\lambda}(R)$ and $V^+(R)$ are the potential curves for the neutral Rydberg state and the corresponding ion, respectively. Equation 1 has been generalized to nondegenerate states of polyatomic molecules and to include the effects of ℓ mixing (29), yielding

$$\Gamma_{\nu_i,\ell,\Gamma_e,\lambda,v_i,v_f} = \sum_{\ell'} \frac{2\pi 2\mathcal{R}}{\nu_i^3}\left[\frac{d\mu_{\ell\ell'}^{\Gamma_e}(Q_i)}{dQ_i}\right]^2_{Q_e^+} |\langle\chi_{v_f}(Q)|Q_e^+|\chi_{v_i}(Q)\rangle|^2. \qquad 3.$$

Here the normal coordinate, Q_i, represents a mass-weighted displacement that vanishes at the equilibrium geometry, Γ_e is the rovibronic symmetry of the

molecule, and ℓ' is the symmetry of the ejected electron. In general, the possibility of ℓ mixing results in a nondiagonal quantum defect matrix. Here the diagonal elements of the quantum defect matrix have a similar meaning to those described in Equation 2, whereas the off-diagonal matrix elements characterize the strength of the ℓ-mixing interactions.

Equations 1 and 3 can be broken down into three factors. The first factor of $2\mathcal{R}/\nu^3$ is essentially a normalization factor proportional to the probability of finding the Rydberg electron at close range to the molecular ion core (28, 30). This factor appears because it is only at close range that the electron is moving fast enough to have a significant effect on the motion of the nuclei. The second factor of $\langle \chi_{v_f}(Q)|Q_e^+|\chi_{v_i}(Q)\rangle$, which is squared in these expressions, has units of displacement along the normal coordinate and is related to the amplitude of the vibration (28, 29). For a harmonic oscillator, this expression vanishes unless $\Delta v_i = \pm 1$, and it is this observation that gives rise to the $\Delta v_i = -1$ propensity rule for vibrational autoionization. Finally, the third term contains the derivative of the quantum defect matrix element with respect to the normal mode of interest, evaluated at the equilibrium geometry of the ion. If this term is zero, it implies that the potential curve of the Rydberg state is parallel to that of the ion at the equilibrium geometry, or that the ℓ-mixing interaction is independent of the normal coordinate. In other words, the Rydberg electron does not affect the potential in which the nuclei move, and thus the vibrational-electronic coupling and autoionization rate vanish. On the other hand, nonzero derivatives imply that the Rydberg electron has an effect on the potential of the nuclei, and thus the coupling and autoionization rate are greater. The largest autoionization rates are expected for those states in which the Rydberg orbital and its interactions have the strongest dependence on the molecular geometry. The initial discussion (29) of Equation 3 focused on vibrational autoionization of molecules in nondegenerate electronic states with nondegenerate ion cores, and the discussion in Sections 2–4 is similarly limited. However, Section 5 includes a discussion of degenerate electronic states and the Jahn-Teller interaction in H_3 (31–37).

Equations 1 and 3 are based on approximations to the more complete MQDT description used in quantitative calculations of Rydberg state dynamics. The quantum defect matrix μ_{ij} or, equivalently, the electronic K matrix $[\mu_{ij} = (1/\pi)\tan^{-1} K_{ij}]$ describes all of the interactions between the electron and the core, including those responsible for vibrational autoionization (13–15). These matrices depend parametrically on Q and are generally nondiagonal in ℓ. The size of the $\mu_{\ell\ell'}^{\Gamma_e}(Q)$ matrix depends on the relevant range of ℓ and the number of times the Γ_e symmetry occurs in the resolution of ℓ into the molecular symmetry. For a given geometry, the MQDT secular equation is

$$\left|\tan \pi \nu_\ell \delta_{\ell\ell'} + \tan \pi \mu_{\ell\ell'}^{\Gamma_e}(Q)\right| = 0. \qquad 4.$$

If the quantum defect matrix $\mu_{\ell\ell'}^{\Gamma_e}(Q)$ is known, Equation 4 can be used to determine the bound electronic state energies. For nondegenerate ion-core states (all of the examples discussed here), Equation 4 is the eigenvalue matrix for $\tan \pi \mu_{\ell\ell'}^{\Gamma_e}(Q)$.

If the eigenvalues are denoted $\tan \pi\mu_\alpha$, the Rydberg potential energy curves are given by

$$V_\alpha(Q) = V^+(Q) - \frac{\mathcal{R}}{[n - \mu_\alpha(Q)]^2}. \quad 5.$$

On the other hand, if the potential energy surfaces are known, they can in principle be used to extract the quantum defect matrix as a function of Q (38–40). Here, the important point is that the quantum defect matrix is expected to vary smoothly and slowly with energy (or equivalently, with n). Thus, potential energy surfaces of low-lying states of the molecule can be used to extract quantum defect matrices that can then be used to calculate the energetics and dynamics of the higher-lying states. Similarly, qualitative information about the potential energy surfaces can be used to predict the qualitative aspects of the excited state dynamics. The physical basis of the smooth energy dependence of the quantum defect matrix is that the asymptotic value of the electron kinetic energy is very small compared to its kinetic energy during a close collision with the core, and thus a moderate change in the asymptotic energy is expected to have little effect on the dynamics of the short-range collision.

One fundamental aspect of quantum defect theory is that different electron-ion coupling schemes are appropriate at different electron-ion distances. Fano and coworkers (13, 41, 42) found a way to treat the molecule in the appropriate coupling scheme for different regions by introducing the idea of frame transformations. The quantum defect matrix $\mu^{\Gamma_e}_{\ell\ell'}(Q)$ describes the short-range interactions when the electron is moving very fast relative to the nuclei and a Born-Oppenheimer framework is appropriate. At long range, the electron moves slowly with respect to the nuclei, and this approximation is no longer valid. Instead, the vibrational quantum numbers of the ion core become the good quantum numbers. The idea of frame transformations is that the transition from one coupling scheme to another occurs very rapidly and that the transition can be accurately estimated by the simple projection of one set of quantum numbers onto the other (13, 34). The vibrational frame transformations between Q and v_i are simply the vibrational wavefunctions. Thus, the short-range quantum defect matrix can be transformed to the vibronic quantum defect matrix using

$$\mu_{kk'} = \mu_{\ell v_i \Gamma_i^+, \ell' v_i' \Gamma_i'^+} = \left\langle V_i^+, \Gamma_i^+ \middle| \mu^{\Gamma_e}_{\ell\ell'} \middle| V_i'^+, \Gamma_i'^+ \right\rangle$$

$$= \int dQ_i \chi^*_{v_i^+ \Gamma_i^+}(Q_i)\, \mu^{\Gamma_e}_{\ell\ell'}(Q_i)\, \chi^*_{v_i'^+ \Gamma_i'^+}(Q_i). \quad 6.$$

This vibronic μ matrix can then be used with the corresponding vibronic MQDT equation

$$\left|\tan \pi\nu_k \delta_{kk'} + \tan \pi\mu^{\Gamma_e}_{kk'}(Q)\right| = 0 \quad 7.$$

to deduce the autoionization widths and profiles.

The appropriate description of the rotational-electronic coupling also depends on the electron-ion distance. At short range, the electron motion is fast relative to the rotational motion of the nuclei, and the projection of the orbital angular momentum onto the molecular frame, Λ, is a good quantum number. This corresponds to Hund's case b. At long range, the electron motion is slow relative to the rotational motion, and Λ is no longer good. Here, the rotational quantum numbers of the ion core are good quantum numbers, corresponding to Hund's case d. The frame transformation is simply the transformation between the two Hund's cases (41). With the inclusion of rotations, the lab frame quantum defect matrix can be written (15) in terms of the molecular frame matrix as

$$\mu_{v_i N_i^+ \Gamma_i^+, v_j^+ N_j^+ \Gamma_{j^+}} = \sum_{\ell,\ell',\Gamma_e,\Lambda} \langle N_i^+ | \Lambda \rangle \int dQ \chi^*_{v_i^+ \Gamma_i^+}(Q) \mu^{\Gamma_e}_{\ell\ell'}(Q) \chi^*_{v_j^+ \Gamma_j^+}(Q) \langle \Lambda | N_j^+ \rangle. \quad 8.$$

The right-hand side of this equation is a step-by-step description of the electron-ion collision. Reading from the right, as the electron approaches the core and picks up speed, it is projected first from Hund's case d to case b, freezing the rotational motion. Then, as the electron further accelerates, it is projected into the Born-Oppenheimer frame, effectively freezing the motion of the nuclei. The electron then undergoes scattering with the core electrons and nuclei, as characterized by the electronic, molecular-frame μ matrix. This matrix can mix states with different values of ℓ, so long as the molecular representation, Γ_e, is conserved. As the electron leaves the core, it is projected back onto the vibrational wavefunctions of the ion. If the electronic molecular-frame μ matrix elements are independent of Q, the matrix can be factored outside the vibrational wavefunctions. Since the vibrational wavefunctions are orthogonal, they will vanish then unless $v_i = v_j$, and vibrationally inelastic processes will not occur. Thus, as discussed above, it is the Q-dependence of the quantum defects that drive the vibrational autoionization process. (Equations 1 and 3 are based on a Taylor's series expansion of the quantum defect with respect to R or Q.) Finally, the electron is projected back from case b to the asymptotic case d rotational levels, which can lead to rotationally inelastic scattering as well.

Equations 1 and 3 indicate that vibrational autoionization will be particularly fast for states in which the Rydberg orbital energy varies rapidly as the molecule is distorted along the normal coordinate of interest. Calculations of the low-lying Rydberg state potential surfaces can be used to determine the quantum defect matrix elements, which can in turn be used to calculate the properties of the higher Rydberg states. Section 5 illustrates this approach for H_3, for which high-level quantum mechanical calculations were performed on the $n = 3$–5 npa_2'' and npe' Rydberg state surfaces and then used as input for MQDT studies of the higher-lying states (31–37, 43). An MQDT study of a limited number of Rydberg states of NO_2 has also been based on quantum chemical calculations of low-lying Rydberg states (44). Unfortunately, such calculations of excited state surfaces are quite difficult, and currently it is worthwhile exploring more qualitative approaches toward understanding the mode dependence of vibrational autoionization.

In a classic series of papers (45–47), Mulliken discussed the behavior of molecular Rydberg states and, in particular, how to infer the behavior of higher-n orbitals from that of low-n orbitals. As n is increased within a given Rydberg series, the angular part of each successive wavefunction remains the same, and the approximate radial function can be generated through the addition of a new radial node and a new loop at large r (45). Aside from a normalization factor of $\nu^{-3/2}$, the innermost loops of the wavefunction vary only slightly with n, which is another way of saying that the molecular frame quantum defect matrix varies slowly with n. Thus, the geometry dependence of the low-n orbitals contains the information necessary to understand the behavior of the high-n states. Mulliken then developed the idea of precursors (45). A Rydberg orbital has a real precursor if the atom or molecule has an occupied valence orbital of the same symmetry, and the short-range behavior of the Rydberg orbital will reflect the behavior of the precursor. Rydberg orbitals with real precursors are expected to be penetrating, i.e., they will have significant amplitude near the core and, in general, relatively large quantum defects. Because unoccupied valence orbitals also have significant amplitude near the atomic nuclei, Rydberg orbitals with the same symmetry as these valence orbitals and lying above them in energy are also expected to be penetrating. Rydberg orbitals with symmetries having no real or virtual valence orbitals as precursors correspond to nonpenetrating orbitals and will generally have small quantum defects (45). Because a nonpenetrating electron never experiences the close collision with the core that is necessary for efficient vibrational to electronic energy transfer, such states are expected to have relatively small vibrational autoionization rates. (Although vibrational autoionization can occur through long-range interactions, this process is generally much slower than autoionization involving the short-range interactions.) It should be noted, however, that motion along a nontotally symmetric vibration can result in a nonpenetrating orbital with no real precursors acquiring penetrating character through interactions that arise as a result of the reduction in symmetry.

Penetrating orbitals may or may not be associated with rapid vibrational autoionization, depending on their variation with geometry. Mulliken also addressed this issue in diatomic molecules, referring to orbitals whose principal quantum number increased by one (or more) in going from separated atoms to united atoms as promoted orbitals and to those whose quantum numbers do not change as unpromoted (45, 46). The simplest example of this concept (46) is found in the $2p\sigma_u$ and $2p\pi_u$ molecular orbitals of H_2. The former is constructed as the subtractive linear combination of $1s_g$ atomic orbitals and is thus promoted. The $2p\pi_u$ orbital is formed from an additive linear combination of $2p_u$ orbitals and is thus unpromoted. Note that the separation of the $2p\sigma_u$ united atom orbital to the $1s_g$ separated atoms results in an increase in the quantum defect of the molecular orbital of 1, whereas the separation of the $2p\pi_u$ orbital united atom orbital results in no change in the quantum defect.

Although promoted orbitals must undergo a large change in quantum defect as a function of geometry, this change must occur near the equilibrium geometry to drive efficient vibrational autoionization. Although nonpenetrating orbitals are

often promoted (45–47), this promotion generally occurs at very large internuclear distances and thus has a minimal effect on the decay dynamics. In the case of H_2, the promotion of the $2p\sigma_u$ orbital does occur close to the equilibrium geometry of the molecule, and the autoionization rate of the $np\sigma_u$ Rydberg states is expected to be large (28, 46, 48). In contrast, the quantum defect of the $2p\pi_u$ state changes very slowly with R, and the autoionization rate of the $np\pi_u$ states is expected to be small. Numerous experiments demonstrate that these expectations are clearly met (21–23).

For diatomic molecules, correlation diagrams show how the orbital energies change in going from separated atoms to united atoms (1, 2, 48). More generally, in polyatomic molecules, Walsh diagrams (3, 4) show how orbital energies change as the molecule is distorted along a particular normal coordinate. Such diagrams clearly show which orbital energies depend strongly on particular vibrations and which orbital energies are only weakly dependent on geometry. Although qualitative Walsh diagrams (and correlation diagrams in general) thus indicate which orbitals will depend most strongly on a given vibration, they do not always indicate at which geometries the energy dependence is greatest. Several investigators, including Buenker and Peyerimhoff, worked extensively in the 1970s to put Walsh diagrams on a more quantitative footing through the use of ab initio calculations (4). As discussed in Section 4, such calculations can provide more insight into the geometries at which the orbital energies change most rapidly. A connection between the orbital energies plotted in the Walsh diagrams and the quantum defects of Equations 1–8 is clear, but the rigorous details remain to be explored. To the extent that the low-n orbitals accurately describe the short-range electron-ion interaction, the orbital energies plotted in the Walsh diagrams are related to the diagonalized μ_α's. That is, at least qualitatively, these curves take into account all of the ℓ mixing, configuration interaction, and even Renner-Teller and Jahn-Teller interactions that may be important. The simple orbital picture will not be valid for all molecules and will tend to break down as a result of major configuration mixings for significant distortions of the molecule. However, for the relatively small displacements from the equilibrium geometry relevant to vibrational autoionization, this viewpoint is useful. The following sections show how these ideas can provide insight into the vibrational autoionization of NH_3, NO_2, and H_3.

In using Walsh diagrams to estimate the Q dependence of the quantum defects of different Rydberg orbitals, it is assumed that the quantum defects are independent of energy. Of course, the quantum defects do display some energy dependence, and this must be taken into account to achieve quantitative agreement theory and experiment (13–15). Typically, the energy dependence is characterized by performing calculations for the first several Rydberg orbitals of the symmetry of interest. By using Walsh diagrams to estimate the behavior of the Rydberg orbitals, the energy-dependence problem is ignored. However, the present discussion is focused primarily on how the orbital energy changes with geometry, and the general trends observed in the Walsh diagrams are expected to be preserved in the Rydberg orbitals.

3. SYMMETRIC STRETCH VS. UMBRELLA BEND IN NH_3

One approach to studying the mode dependence of vibrational autoionization in polyatomic molecules is to excite a Rydberg series converging to an ionic limit in which two different vibrational modes are excited, and to use photoelectron spectroscopy to determine the relative populations of the ionic vibrational levels when the Rydberg electron autoionizes (49). If the Rydberg state has sufficient energy to autoionize via a $\Delta v_i = -1$ process for either normal mode, and if the propensity rule holds, the relative intensities of the corresponding photoelectron peaks provide information on the relative rates of the two autoionization pathways. As an example, double-resonance excitation via the low-lying C′ $3pa_2''\ ^1A_1'$ (1300) Rydberg state (50) of NH_3 was used to prepare autoionizing Rydberg states converging to the $NH_3^+(1300)$ threshold. Here the vibrational quantum numbers (v_1, v_2, v_3, v_4) correspond to the symmetric stretch, umbrella bend, in-plane asymmetric stretch, and in-plane asymmetric bend, respectively, for the planar Rydberg states and ground state ion. (Although the electronic ground state of NH_3 is pyramidal, the electronic ground state of NH_3^+ and the Rydberg series converging to it are planar.) Above the NH_3^+ X $^2A_2''(1200)$ limit, these series can autoionize by $\Delta v_1 = -1$ or $\Delta v_2 = -1$ processes into the X $^2A_2''(0300)$ or (1200) continua, respectively. The relative intensities of these two peaks in the angle-integrated photoelectron spectrum then provide a determination of the relative autoionization probabilities for the $\Delta v_1 = -1$ or $\Delta v_2 = -1$ processes, respectively.

The experiments on NH_3 were performed in a supersonic molecular beam of NH_3 in He (49). The C′ $3pa_2''\ ^1A_1'$ (1300) level was populated by a two-photon transition from the ground state using a frequency-doubled, pulsed Nd:YAG-pumped dye laser. A second Nd:YAG-pumped dye laser was used to probe transitions from the intermediate level to the energy region of interest. Scanning the probe laser with the pump laser fixed and while monitoring the total electron signal (or total ion signal) provided a spectrum of the autoionizing resonances (49), such as that shown in Figure 2. The probe laser was then tuned to the resonance of interest and the photoelectron spectrum was recorded by using a magnetic bottle electron spectrometer. This spectrometer has the advantage of ~50% collection efficiency, and it removes the need for correcting the branching fractions for the photoelectron angular distributions. The magnetic field of this instrument can affect the autoionization dynamics at high principal quantum number ($n > \sim 25$), but the spectra reported here were obtained at moderate n, where such effects are expected to be minor.

Although a detailed rotational assignment of the spectrum in Figure 2 has not yet been made, the series of labeled resonances is expected to correspond to an nda_1' or nde'' series (49). Photoelectron spectra for the $n = 11$–14 members of this series, which all lie above the NH_3^+ X $^2A_2''$ (1200) and (0300) thresholds, are shown in Figure 3. The photoelectron spectra for all five levels are very similar, with relative peak intensities that are nearly independent of n. All of the spectra are dominated by an intense doublet feature at low energy, which has been assigned (49) to the

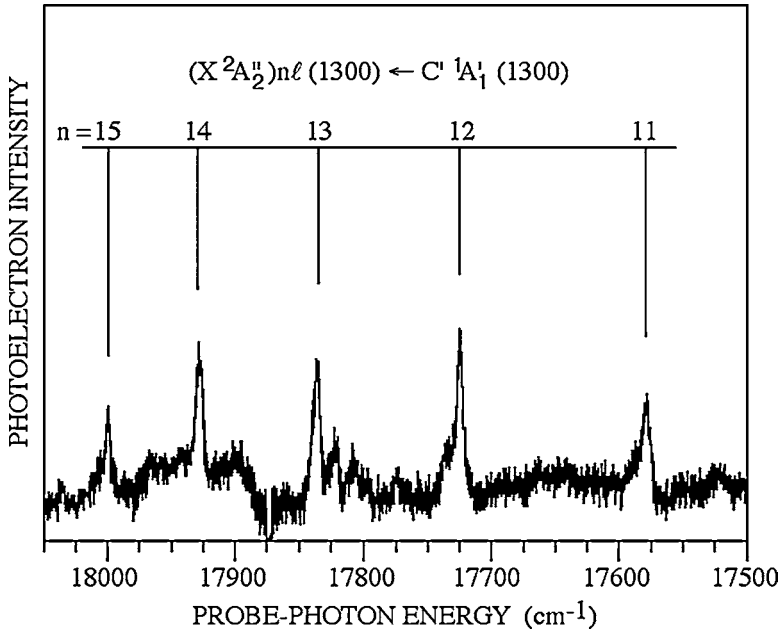

Figure 2 Wavelength scan of NH_3 obtained by pumping the C′ $^1A_1'$ (1300) vibronic level and probing in the region between the NH_3^+ X $^2A_2''$ (1200) and (1300) thresholds. From Reference 49, used with permission from the authors and the American Institute of Physics.

population of different rotational levels within the X $^2A_2''$ (1200) ionic state. This feature accounts for 70–80% of the integrated intensity in all of the spectra. In contrast, the photoelectron peak corresponding to the population of the (0300) state is always very small. Taken together, the spectra indicate that autoionization via the umbrella bend ($\Delta v_2 = -1$) is much more efficient than ionization via the symmetric stretch ($\Delta v_1 = -1$). In addition, all of the remaining peaks in Figure 3 are also quite small; this observation is consistent with the vibrational propensity rule because all of these peaks require processes with $\Delta v_{total} = 2$ or higher.

Assuming the short-range radial wavefunctions are similar for the low and high Rydberg states, the effect of displacements on the nda$_1'$ and nde$''$ orbital energies can be estimated by examining the angular character of the Rydberg wavefunction. The nda$_1'$ orbital corresponds to the d_{z^2} orbital, symmetrized for D_{3h}. This orbital has positive lobes along the symmetry axis with a node at the origin, along with a doughnut-shaped lobe of opposite sign lying in the molecular plane (51). The nde$''$ orbital corresponds to a symmetrized linear combination of the d_{xz} and d_{yz} orbitals, with a nodal plane corresponding to the plane of the molecule. The normal mode dependence of these orbitals can be estimated from the qualitative Walsh

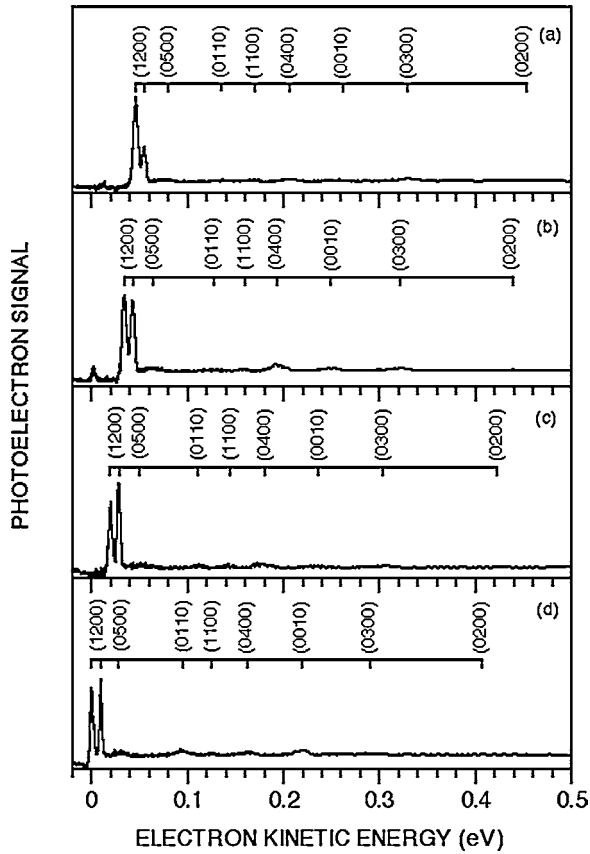

Figure 3 Photoelectron spectra obtained for some of the resonances in Figure 2: (*a*) n = 14, (*b*) n = 13, (*c*) n = 12, (*d*) n = 11. From Reference 49, used with permission from the authors and the American Institute of Physics.

diagrams for the symmetric stretch and umbrella bend of NH_3 (5), which are shown in Figure 4. The orbitals shown in the figure are not generally described by a single value of ℓ, and they are closer to the α channels discussed in Section 2; nevertheless, it is often possible to associate a dominant value of ℓ to these orbitals.

The nde″ orbital is considered first. There are no orbitals with e″ symmetry in Figure 4, indicating that there are no real precursors for the nde″ orbital in the planar geometry. Thus, this is nominally a nonpenetrating orbital and remains nonpenetrating along the symmetric stretch. Furthermore, the nuclei of the molecule lie in a nodal plane of the orbital, and as a result, the orbital energy is not expected to depend significantly on the symmetric stretching coordinate. Vibrational autoionization via $\Delta v_1 = -1$ is therefore expected to be slow for this series. Along the nontotally symmetric umbrella mode, the D_{3h} symmetry of the molecule breaks,

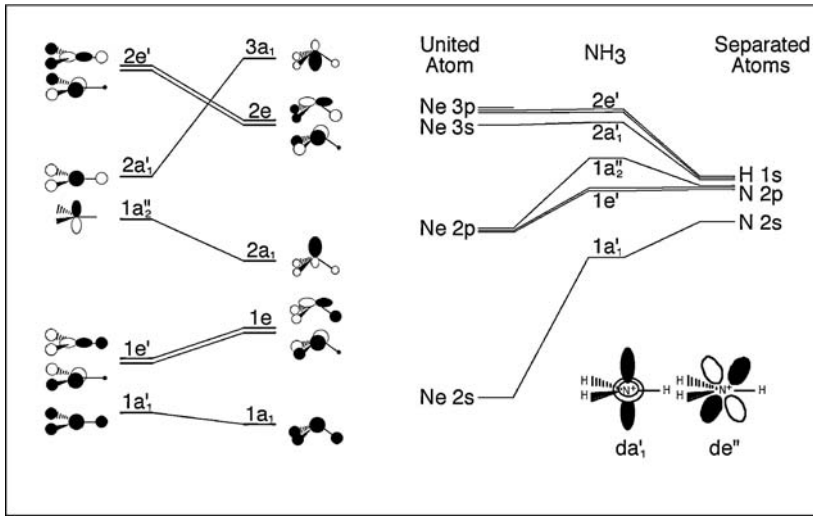

Figure 4 Walsh diagrams for NH_3 along the umbrella bend and symmetric stretch (planar NH_3). The diagram for the umbrella mode is adapted from Reference 5, with permission of Oxford University Press, Inc.

and the nde″ orbital reduces to nde in C_{3v} symmetry (52); the latter orbital does have precursors in NH_3, and thus penetrating character is acquired as the molecule bends. In the pyramidal geometry, the e″ and e′ orbitals from D_{3h} mix, as is clear from the similarity of some of the e orbitals on the right-hand side of Figure 4 with atomic d_{xz} and d_{yz} orbitals. The large change of orbital energy of the e′/e orbital in Figure 4 along the umbrella coordinate (3) is expected to be reflected in a complementary change in the orbital energy of the e″/e orbital. Thus, the quantum defect for the de″ orbital is expected to change substantially along the umbrella coordinate, resulting in efficient vibrational autoionization.

In contrast to the nde″ orbital, the nda_1' orbital does have a real precursor in the $1a_1'$ orbital and an unoccupied valence precursor in the $2a_1'$ orbital. However, the Walsh diagram in Figure 4 indicates that the orbital energy of the $2a_1'$ orbital is very close to that for the united atom Ne 3s orbital, indicating that it is fully promoted at the equilibrium geometry of NH_3. To the extent that the united atom labels apply, the d orbitals are orthogonal to the s orbitals. Thus, the d orbitals do not have any real precursors, because the 3d orbital is unoccupied in the ground state of Ne and NH_3. This argument for nonpenetrating character is consistent with the very small, slightly positive quantum defect of ∼0.006 observed for the $3da_1'$ Rydberg state of NH_3 (53). In addition, to the extent that the promotion occurs at relatively large NH distances, the $3nda_1'$ quantum defect and its derivatives are expected to remain small for small displacements along the symmetric stretching coordinate. Thus, autoionization of nda_1' Rydberg states via this vibrational mode is expected to be slow.

Figure 4 shows that as the molecule is bent along the umbrella coordinate, the energy of the $2a_1'$ orbital increases significantly. The reduction of symmetry, or, from another perspective, the dipole moment produced by the bending, results in mixing between the a_1' and a_2'' states. Thus, the schematic orbital diagrams show the $2a_1'$ orbital acquires $1a_2''$ character as the molecule is bent. Similar mixing with the $1a_2''$ and higher a_2'' orbitals will also occur for the higher a_1' orbitals more closely associated with the nda_1' series. This mixing will give the nda_1' orbitals significantly more penetrating character. As a result, the relevant μ_α's for the nda_1' Rydberg states are expected to depend on the umbrella mode and thus drive vibrational autoionization. Although the Walsh diagrams plot something related to the μ_α's discussed in Section 2, it is clear that the $\mu_{pd}^{a_1}(Q)$ and $\mu_{sp}^{a_1}(Q)$ will also vary substantially along the umbrella coordinate.

4. SYMMETRIC STRETCH VS. BEND IN NO_2

In a series of experiments, Grant and coworkers (54–59) examined the vibrational mode dependence of the spectroscopy and dynamics of linear Rydberg states of NO_2 converging to vibrationally excited levels of the linear $X\,^1\Sigma_g^+$ ground state of NO_2^+. In their three-color experiments (55–59), the first color was resonant with a transition from the bent $^2A_1$ ground state to a vibronic level in a complex region containing three strongly interacting electronic states, and the second color was resonant with a transition from this selected level to a single vibronic level of the $3p\sigma_u$ Rydberg state. Although the detailed nature of the state accessed at the one-photon energy has not been characterized, the double-resonance process allowed the assignment of the rotational quantum numbers in both this state and the $3p\sigma_u$ Rydberg state (55–59). With these two colors fixed, the third color was then tuned to map out transitions from the $3p\sigma_u$ state to the autoionizing Rydberg states of interest. An example of these spectra is shown in Figure 5. Because the potential surfaces of the $3p\sigma_u$ state and the higher lying Rydberg states converging to the $X\,^1\Sigma_g^+$ state are similar, Franck-Condon factors strongly favor the preservation of the vibrational quantum numbers in the transition driven by the third color. The dominant transitions from the $3p\sigma_u$ state are expected to be to the $ns\sigma_g$, $nd\sigma_g$, and $nd\pi_g$ Rydberg series, and Grant and coworkers assigned these and other weaker series on the basis of this expectation and the observed quantum defects of the series (55–59). By recording spectra via the $3p\sigma_u$ ($v_1 = 0-3$; $v_2 = 0$; $v_3 = 0$), (0; $v_2 = 1, 2$; 0), and (001) levels, Bryant et al. were able to compare the linewidths of the autoionizing series as a function of their vibrational quantum numbers (57). [Here, (v_1, v_2, v_3) correspond to the symmetric stretch, bend, and asymmetric stretch, respectively.] For the three dominant series, they found that the symmetric stretching mode resulted in the largest linewidths, followed by the asymmetric stretching mode, and, finally, the bending mode (57). It is assumed the widths correspond to single rotational levels.

One difficulty with linewidth measurements is that it is not always clear what decay path is responsible for the observed width. For example, predissociation

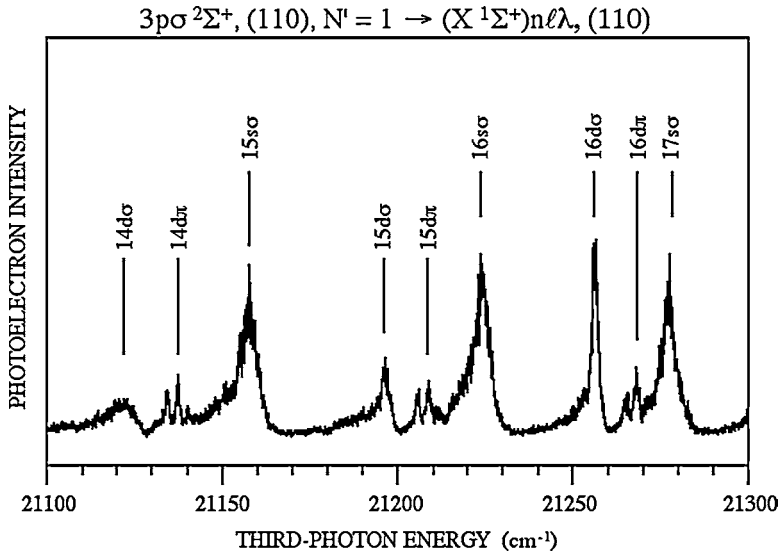

Figure 5 Wavelength scan of NO_2 obtained by pumping the $3p\sigma_u$ (110) level via two-color excitation and probing with a third tunable laser between the NO_2^+ $X\,^1\Sigma_g^+$ (100) and (110) thresholds.

(or another radiationless transition), rather than autoionization, could be responsible for the larger widths of the (v_1, 0, 0) resonances. To address this issue, photoelectron spectra were recorded (60) for Rydberg series converging to the $X\,^1\Sigma_g^+$(110) level of NO_2^+. As illustrated in Figure 5, the three-color spectrum via the $3p\sigma_u$(110) level is very similar to those via the other vibrational levels, allowing the assignments of the dominant series. Above the NO_2^+ $X\,^1\Sigma_g^+$(100) threshold, the (110) Rydberg series can decay by $\Delta v_1 = -1$ and $\Delta v_2 = -1$ processes, as well as by other processes involving larger changes in the vibrational quantum numbers. As in the NH_3 spectra discussed in Section 3, the relative intensities of the NO_2^+ $X\,^1\Sigma_g^+$(010) and (100) photoelectron peaks provide a direct measure of the relative importance of the $\Delta v_1 = -1$ and $\Delta v_2 = -1$ processes, respectively.

Figure 6 shows the resulting photoelectron spectra for the $15d\sigma_g$ and $14d\pi_g$ Rydberg states of NO_2. These spectra are typical of those recorded for the $ns\sigma_g$, $nd\sigma_g$, and $nd\pi_g$ autoionizing resonances with moderate n and lying above the NO_2^+ $X\,^1\Sigma_g^+$(100) threshold (60). In both spectra, the $X\,^1\Sigma_g^+$(010) photoelectron peak is much more intense than the (100) peak. This observation indicates the $\Delta v_1 = -1$ process is substantially faster than the $\Delta v_2 = -1$ process, in agreement with the conclusions based on the linewidth measurements of Bryant et al. (57).

Recently, Petsalakis et al. (44) have performed MQDT calculations on the $nd\sigma_g$ autoionizing states of NO_2, in which quantum chemical calculations were used to determine the $d\sigma_g$ quantum defect as a function of geometry. Because these calculations were restricted to a single value of ℓ, they could not treat processes

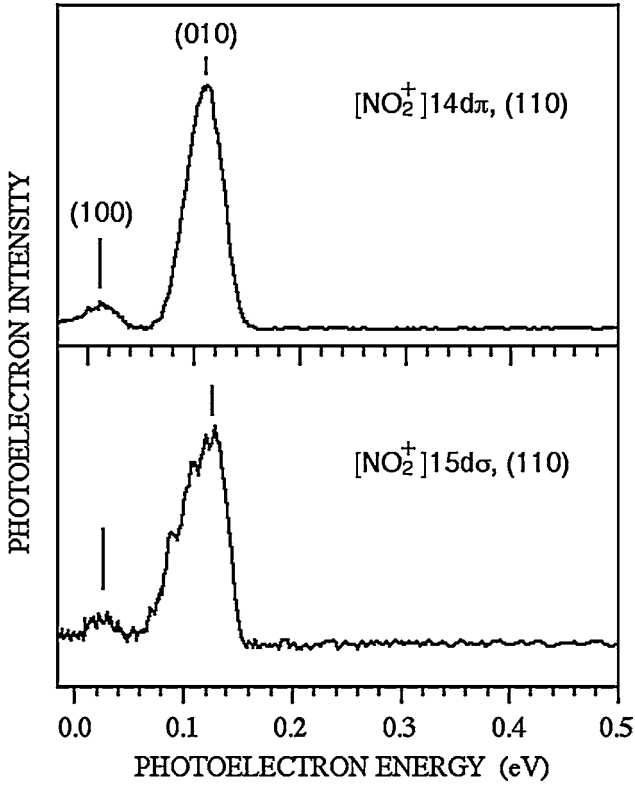

Figure 6 Photoelectron spectra for the $14d\pi_g$ (110) and $15d\sigma_g$ (110) resonances shown in Figure 5.

in which $\Delta v_2 =$ odd or $\Delta v_3 =$ odd (or more generally, in which $\Delta v_2 + \Delta v_3 =$ odd). This restriction arises because the ν_2 and ν_3 vibrations are nontotally symmetric, with ungerade character in the linear molecule (52). Thus, a change in the vibrational symmetry from u $\rightarrow$ g or vice versa must be compensated by a change in the electronic symmetry. In this case, this change in electronic symmetry must correspond to a change in the partial wave of the ejected photoelectron, e.g., decay of the nd Rydberg state with the ejection of a p or f photoelectron, and such processes are not included in the calculation. Processes with $\Delta v_{2,3} =$ even were included in the calculations of Petsalakis et al. (44), but, as expected, were relatively weak. Interestingly, the linewidths calculated for the $nd\sigma_g$ resonances undergoing $\Delta v_1 = -1$ autoionization appear to be in reasonable agreement with experiment (55, 56), thus supporting the conclusions above.

To some extent, these observations can also be rationalized in terms of the qualitative arguments based on Walsh diagrams such as those described above. Unfortunately, such qualitative information is less complete than for NH_3. Figure 7

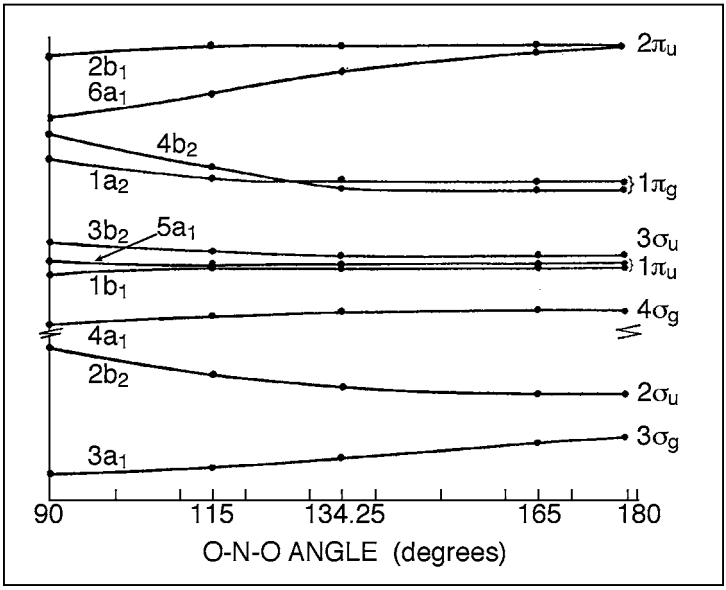

Figure 7 Walsh diagram for the bending coordinate of NO_2 adapted from Reference 61, used with permission from the authors and the American Institute of Physics.

shows an ab initio Walsh diagram calculated for the bending coordinate of NO_2 adapted from Burnelle et al. (61). Although qualitative Walsh diagrams for AB_2 molecules are similar in appearance (3, 7), the ordering of the orbitals is slightly different, as are the detailed shapes. Because the Rydberg states are linear, the behavior of the orbital energies near the linear geometry is most important. As the molecule is bent, the ungerade and gerade states mix, and these mixings are taken into account in the Walsh diagrams.

The $ns\sigma_g$ and $nd\sigma_g$ orbitals have a common precursor in NO_2, corresponding to the $4\sigma_g$ valence orbital. As discussed by Jungen for a similar situation in NO (62), the common precursor is expected to result in significant $s\sigma$-$d\sigma$ mixing, and the nominally $ns\sigma_g$ and $nd\sigma_g$ Rydberg series are expected to have mixed character. Interestingly, although qualitative Walsh diagrams (3, 7) for the $4\sigma_g$ orbital energy show it varying rapidly along the bending coordinate, the corresponding orbital energy in the more quantitative Walsh diagram is nearly constant until the molecule is bent quite significantly. Thus, vibronic coupling via the bending coordinate is expected to be weak for the $ns\sigma_g$ and $nd\sigma_g$ series, as observed in the experiments.

The situation is somewhat more complex for the $nd\pi_g$ orbitals, which have the $1\pi_g$ valence orbital as a precursor. Because this orbital is doubly degenerate, it undergoes Renner-Teller interactions as the molecule is bent (52). This interaction splits the orbital into components with a_2 and b_2 symmetry. The expression given in

Equation 3 has not yet been extended to treat degenerate electronic states, although Staib et al. have treated the Renner-Teller interaction in calculations using MQDT (63). Both the qualitative and quantitative Walsh diagrams show that the splitting is small near the linear geometry, and that the orbital energies vary only slightly for small displacements along the bending coordinate. These observations indicate that the coupling of the ndπ_g series to the bending vibration will again be weak, as is observed in the experiment. Although such qualitative considerations appear to be consistent with observations in NO_2, more extensive MQDT calculations that include multiple values of ℓ and incorporate the Renner-Teller interaction explicitly are likely to provide considerable insight into the decay dynamics of this prototypical triatomic molecule.

5. VIBRATIONAL AUTOIONIZATION OF H_3

The photoionization dynamics of H_3 should be simpler than those of any other polyatomic molecule. Nevertheless, experimental (43, 64–74) and theoretical (31–37) studies have revealed a number of interesting results, in particular the importance of the Jahn-Teller effect in the autoionization of Rydberg states of H_3. Although the electronic ground state of H_3 is repulsive, that of H_3^+ is fairly strongly bound. As a result, Rydberg states based on the ground state of H_3^+ can be long-lived, even though all are ultimately unstable with respect to dissociation to $H_2 + H$. Herzberg was the first to observe the emission spectrum of H_3 in electric discharges (64–66), where the spectrum corresponds to transitions between Rydberg states. Gellene & Porter demonstrated that neutral excited states of H_3 could be formed by charge exchange reactions in fast ion beams (67). Somewhat later, Walther and coworkers used this approach to study the emission spectrum of H_3 Rydberg states (68–70). Helm (71) then demonstrated that photoabsorption spectra of H_3 in neutralized fast ion beams could be recorded by probing transitions from the single long-lived $N = K = 0$ rotational level of the B 2p $^2A_2''$ state. This state corresponds to the ground electronic state of H_3^+ plus a $2pa_2''$ electron in an orbital perpendicular to the plane of the equilateral triangle of the nuclei. Although higher rotational levels of the B state are predissociated by rotational coupling to the dissociation continuum of the X 2p $^2E'$ ground state, this process is inoperable for the B 2p $^2A_2''$ $N = K = 0$ level, as there is no $N = K = 0$ level of the ground state with which to couple. Several groups (43, 72–75) have made use of this single stable level to probe the higher lying Rydberg structure of H_3; the most extensive studies have been performed by Helm and coworkers.

The $2pa_2''$ orbital has nearly pure p character, and initial single-photon excitation studies probed transitions to the ns and nd Rydberg states. Soon thereafter, Lembo et al. (73) used two-color, two-photon excitation from the B 2p $^2A_2''$, $v_1 = 0$, $v_2{}^l = 0^\circ$, $N = K = 0$ level to characterize transitions to the high-lying nf Rydberg states, and Bordas et al. (74) used a similar approach to perform an extensive study of the np Rydberg states. Here ν_1 corresponds to the symmetric stretch, ν_2

corresponds to the degenerate asymmetric stretch/bend, and l corresponds to the vibrational angular momentum in ν_2; these are abbreviated (v_1, v_2^l) below. In the latter study (74), the first color was used to pump the 3s $^2A_1'$ (0, 0°), N = 1, K = 0 ← B 2p $^2A_2''$, (0, 0°), N = K = 0, and the second color was used to probe transitions from the 3s state to the region of the first ionization threshold. Bordas et al. (74) observed bound states converging to the lowest ionization threshold, rotationally autoionizing states converging to rotationally excited levels of the ground vibrational state, and vibrational autoionization of Rydberg states based on excited vibrational levels of H_3^+. Reichle et al. (75) and Mistrik et al. (43) later performed more extensive studies of the autoionizing np Rydberg series by using the same approach and the 3s $^2A_1'$ (1, 0°), N = 1, K = 0 intermediate state. The results on the np Rydberg series have been the subject of several theoretical studies based on MQDT (31–37, 43), and the present discussion is focused on these results.

The B 2p $^2A_2''$, $v_1 = 0$, $v_2^l = 0°$, N = K = 0 level is an ortho-nuclear spin state, and because the nuclear spin does not change in an electric dipole transition, the 3s $^2A_1'$ (v_1, 0°), N = 1, K = 0 levels, and the Rydberg levels excited from them, also have ortho character (71, 73–76). The H_3^+ levels populated by the photoionization of ortho H_3 will also have ortho character. The Rydberg series excited from the 3s (v_1, 0°), N = 1, K = 0 level have N = 0, 1, and 2, and Helm and coworkers determined the value of N for each observed series by recording spectra with different relative polarizations of the pump and probe lasers (43, 73–75). Although the intermediate level belongs to a 3s Rydberg state and the dominant transitions are to np Rydberg series, some transitions to nd Rydberg states have also been identified in the spectra; these arise from the nonspherical nature of the molecular 3s state (43, 73–75). To date, theoretical analyses have focused on the np series alone (31–37) and ignored ℓ mixing with other series. The present discussion follows this lead.

For N = 0, there is a single allowed np Rydberg series converging to the N^+ = 1 level of each (v_1, v_2°) level of the ion (32–34, 43). (Note that $\ell_v = 0$ requires v_2 = even.) In the absence of ℓ mixing, these series have pure npa_2'' character; that is, the Rydberg electron is in a p_z orbital perpendicular to the plane of the molecule. The occupied valence orbitals of H_3 correspond to the $1sa_1'$ and $2pe'$ orbitals, and there are no precursor orbitals with a_2'' symmetry. Thus, the npa_2'' orbitals are expected to be nonpenetrating, which is consistent with the observed quantum defect of 0.06 at the equilibrium geometry. Near the equilibrium geometry, motion along the symmetric stretch is not expected to result in a significant change in the orbital energy. This is consistent with the quantum defect plot of Mistrik et al. (43), which shows that the $4p_z$ quantum defect changes by only 0.03 following a displacement of ~0.4 a_0 along the symmetric stretch. Thus, the $\Delta v_1 = -1$ autoionization process is not expected to be fast.

For symmetry reasons, the first derivative of the pa_2'' quantum defect at the equilibrium geometry vanishes along the e′ asymmetric stretch/bend (43). Put another way, the $\Delta v_2 = -1$ process changes the vibrational symmetry by a factor of e′, which requires compensation by a change in either the electronic or rotational

symmetry of the total system (52). In the absence of ℓ mixing, this is not possible for $N = 0$ levels, as no rotational or electronic levels of the required symmetry exist. Thus, for the npa_2'', $N = 0$ states, the vibrational autoionization rate for ν_2 is expected to be very small. Autoionization processes with $\Delta v_2 = -2$ can avoid such symmetry problems, as the $e' \otimes e'$ direct product contains the totally symmetric representation (52). However, such $\Delta v_2 = -2$ processes require quadratic terms in the interaction matrix element, and the vibrational propensity rule suggests that such processes will be very slow (8, 29). Figure 8 shows the linewidths of three $N = 0$ resonances from Mistrik et al. (43). The 9p $(0, 2^\circ)$ resonance in Figure 8*a* requires such a $\Delta v_2 = -2$ process, and as expected, it is extremely sharp. The other two resonances correspond to 7p $(2, 0^\circ)$ and 8p $(2, 0^\circ)$, and these can decay into the H_3^+ $(v_1 = 0,1; v_2{}^l = 0^\circ)$ $N^+ = 1, K^+ = 0$ continua. Although the lineshapes in Figures 8*b* and 8*c* can be resolved, the resonances are still relatively sharp considering the low values of n^*. As expected, this indicates that even vibrational autoionization via ν_1 is not too efficient for the npa_2'' series in H_3.

In the absence of ℓ mixing, the only allowed np Rydberg series that exists with $N = 1$ is the npe′ series (32–34, 43). The npe′ orbital is doubly degenerate, with a projection of $\Lambda = \pm 1$ on the symmetry axis of the molecule. One npe′ series converges to the $N^+ = 1, K^+ = 0$ level of each $(v_1, v_2{}^\circ)$ level of the ground state of H_3^+. In addition, one such series also converges to the $N^+ = 2, K^+ = 2$ level of every $(v_1, v_2{}^1)$ level. The npe′ orbital lies in the plane of the three hydrogen atoms, and because the 2pe′ valence orbital is the precursor to the npe′ orbitals, the npe′ orbitals are expected to be penetrating. This expectation is met, as indicated by the relatively large equilibrium value of the pe′ quantum defect of ~0.4 (43).

Because the npe′ orbital is degenerate, the Jahn-Teller effect is important with respect to distortion along the asymmetric stretch/bend coordinate, which also has e′ symmetry (31–34, 52). At the symmetric geometry, the in-plane p_x and p_y orbitals are degenerate and together make up the pe′ orbital. As the molecule is distorted along ν_2, however, the orbitals split. The p_x and p_y orbital energies show a linear dependence on the displacement along ν_2, and the corresponding quantum defects depend strongly on this displacement, leading to substantial vibronic interactions.

Interestingly, whereas the npe′ series converging to the H_3^+ $(v_1 > 0, v_2{}^\circ)$ $N^+ = 1, K^+ = 0$ levels can autoionize just as the $N = 0$, npa_2'' series do by $\Delta v_1 = -1$ processes, the npe′ series converging to the $(v_1, v_2{}^1)$ $N^+ = 2, K^+ = 2$ levels can autoionize by a $\Delta v_2 = -1$ process that is forbidden for the np a_2'' series (31–34). This process is driven by the Jahn-Teller interaction and can be viewed as an npe′, $\Lambda = \pm 1$ electron scattering off the H_3^+ $(v_1, v_2{}^1)$ $N^+ = 2, K^+ = 2$ core and de-exciting it to the H_3^+ $(v_1, (v_2\text{-}1)^0)$ $N^+ = 1, K^+ = 0$ level, with a concurrent flip of $\Lambda = \pm 1$ to $\Lambda = \mp 1$. The overall rovibronic symmetry of the electron-ion complex is preserved in this process: Even though the vibrational symmetry changes by a factor of e′ (through the loss of one quantum of the e′ vibration), the rotational symmetry also changes by a factor of e′ in going from $K^+ = 2$ to $K^+ = 0$. The important point is that the Jahn-Teller interaction provides a mechanism for efficient vibrational autoionization via nontotally symmetric vibrations (31). Thus,

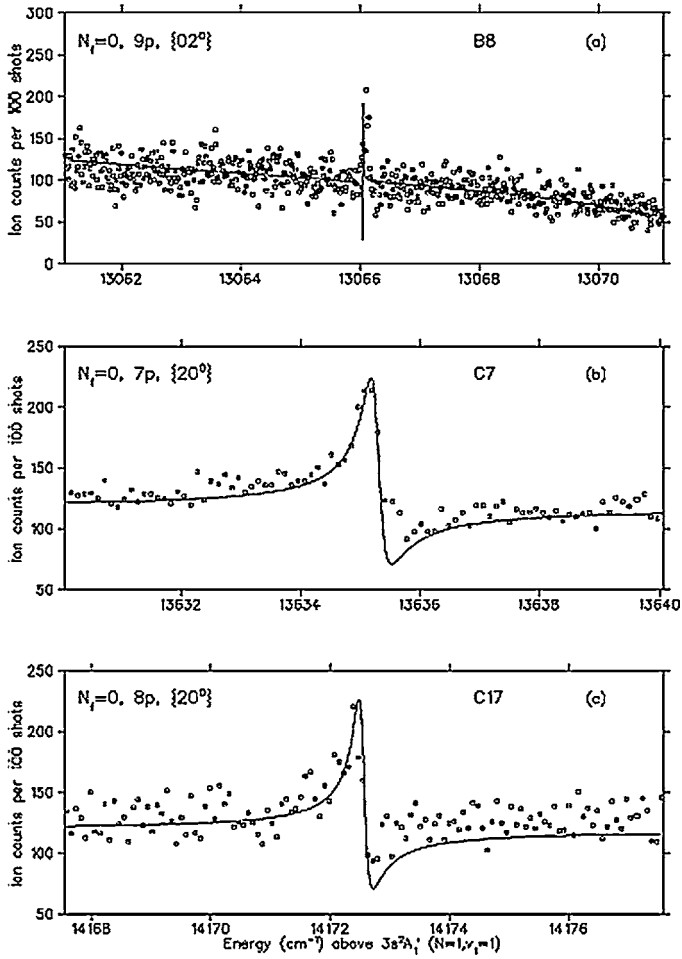

Figure 8 Lineshapes for selected npa_2'', $N = 0$ resonances of H_3. Reprinted from Reference 43 with permission from the authors and the American Physical Society. Copyright 2000 by the American Physical Society.

for the npe' series, resonances analogous to the extremely sharp npa_2'' resonance in Figure 8*a* can actually decay quite rapidly.

The np, $N = 0$ and 1 series are particularly simple because, in the absence of ℓ mixing, they correspond to pure npa_2'' and npe' series, respectively (32–34). As shown in Figure 9, for $N = 2$, both npa_2'' and npe' series exist, and these interact through rotational ℓ uncoupling (32–37). For (v_1, v_2°) levels, one of the ℓ-uncoupled $N = 2$ series converges to the corresponding $N^+ = 1, K^+ = 0$ level and one converges to the $N^+ = 3$, $K^+ = 0$ level. For (v_1, v_2^1) levels, one of the $N = 2$ series converges to the $N^+ = 2$, $K^+ = 2$ level and one converges to the

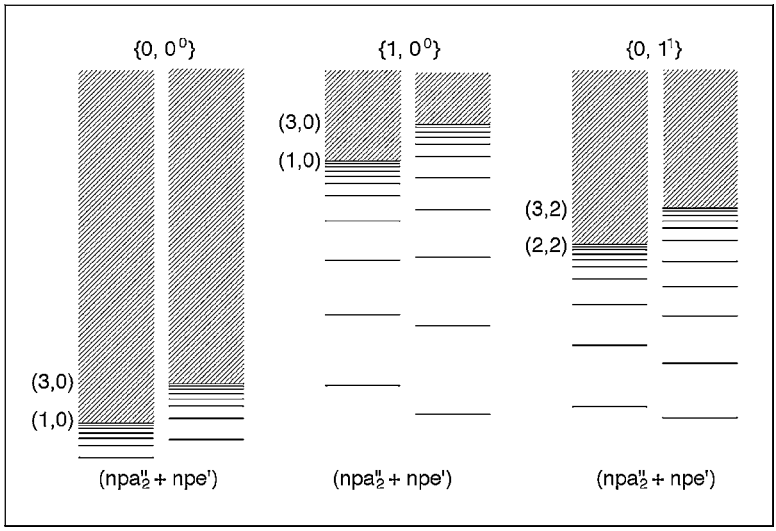

Figure 9 Schematic diagram of npa_2'' and npe′, N = 2 Rydberg states of H_3 and the corresponding levels of H_3^+ to which they converge.

$N^+ = 3, K^+ = 2$ level. The resulting spectra are complex, and in the absence of a theoretical model that includes both these rotational interactions and the Jahn-Teller coupling, many of the assignments are difficult. The Jahn-Teller interaction was first incorporated into MQDT by Staib & Domcke (31), who introduced a geometry-dependent, molecular frame reaction matrix based on the earlier work of Longuet-Higgins (77). This approach was then used by Stephens & Greene (32–34) in more quantitative calculations of the H_3 spectrum and was recently modified and extended by Kokoouline & Greene (35–37) to include the possibility of predissociation. For the np, N = 2 series, the reaction matrix corresponds to the 3 × 3 matrix[2] (31–37, 43, 78)

$$K_{\Lambda\Lambda'}(Q) = \begin{array}{c} \\ \Lambda = 0 \\ \Lambda = 1 \\ \Lambda = -1 \end{array} \begin{array}{c} \begin{array}{ccc} \Lambda' = 0 & \Lambda' = 1 & \Lambda' = -1 \end{array} \\ \begin{pmatrix} \tan[\pi\mu_{\Lambda=0}(Q)] & 0 & 0 \\ 0 & \delta\rho^2 & \lambda\rho\exp(i\phi) \\ 0 & \lambda\rho\exp(-i\phi) & \delta\rho^2 \end{pmatrix} \end{array}. \quad 9.$$

Here, λ and δ are the linear Jahn-Teller splitting parameter and frequency shift parameter, respectively, and ρ and φ are the radial and azimuthal coordinates describing the ν_2 coordinate (43). Essentially, ρ describes the magnitudes of the

[2]Reference 36 discusses an inconsistency in the details of the K matrix in some of the earlier references.

displacement and ϕ describes its orientation with respect to the molecular frame (77). The diagonal element $\tan[\pi \mu_{\Lambda=0}(Q)]$ characterizes the core-npa$_2''$ interaction, whereas the off-diagonal elements in the lower right-hand corner couple the two Λ components of the npe$'$ series. The ℓ uncoupling that mixes the np a$_2''$ and npe$'$ channels is included through the use of a rotational frame transformation, as indicated in Equation 8 (32–37, 43, 79).

A comparison of the experimental and theoretical spectra of H_3 is shown in Figure 10. Considering the complexity of the problem, the agreement between experiment and theory is quite impressive. The incorporation of the Jahn-Teller interaction into the MQDT framework allows the assignment of a large number of autoionizing resonances that would otherwise be difficult to assign (32–37, 43). Even when the energies of the resonances are not in perfect accord, assignments can generally be made on the basis of intensities and N values. Because it provides a mechanism for efficient vibrational autoionization via nontotally symmetric vibrations, the Jahn-Teller interaction is expected to play an important role in the photoionization dynamics of many symmetric polyatomic molecules (31, 80, 81). In particular, the Jahn-Teller interaction is expected to be essential for understanding the pe$'$, de$'$, and de$''$ Rydberg states of NH_3 (54, 80). Although the work on H_3 has provided a framework for incorporating the Jahn-Teller interaction into the photoionization dynamics of polyatomic molecules, considerable additional

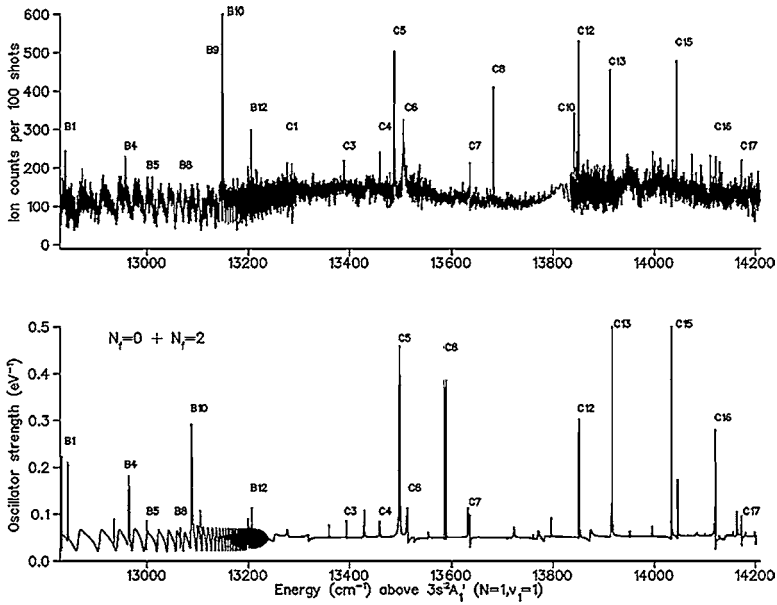

Figure 10 Experimental and theoretical spectra of H_3. From Reference 43 with permission from the authors and the American Physical Society. Copyright 2000 by the American Physical Society.

work is necessary to explore its ramifications in a broader range of systems. By incorporating the Jahn-Teller interaction into the MQDT framework, it is possible to treat full Rydberg series (i.e., an infinite series of conical intersections) and the interactions between them with a small set of dynamical parameters (31–37).

The observation that the Jahn-Teller interaction can dramatically increase the vibrational autoionization rate via nontotally symmetric vibrations also has implications for the inverse process of electron capture by molecular ions. For many years, there was considerable disagreement between experimental and theoretical determinations of the dissociative recombination rate of H_3^+ with low energy electrons. (This process corresponds to the capture of an electron by the H_3^+, followed by dissociation to neutral fragments.) Specifically, the theoretical values were considerably lower than the experimental determinations. By incorporating the Jahn-Teller interaction into their treatment of the dissociative recombination of H_3^+, Kokoouline et al. were able to show that electron capture into np Rydberg states played an important role in the dissociative recombination of H_3^+ and achieved reasonable agreement with experiment for the first time (35, 36).

6. FUTURE DIRECTIONS

The study of vibrational autoionization can provide insight into the coupling of electronic and vibrational motion in polyatomic molecules. Although the process occurs in relatively highly excited Rydberg states, the theoretical perspective of MQDT shows how it is intimately connected to the spectroscopy and dynamics of the lower energy states of the molecule. With this connection, both qualitative and quantitative information on the low-lying states of the molecule can be used to rationalize and predict the behavior of the highly excited states. Turned around, this connection also allows the detailed information generated through the study of highly excited states to be used to provide insight into fundamental and general aspects of vibronic interactions.

This review has emphasized qualitative behavior that can be extracted from relatively simple arguments, as well as general features of the vibrational-electronic coupling. The future clearly lies in more rigorous calculations based on quantum chemical input data and fully developed MQDT analyses. Several significant MQDT studies of the photoionization dynamics of other polyatomic molecules, including H_2O and NH_3 (82–85), have already been performed. Such studies have allowed the assignment of structure in the near-threshold photoionization spectra and in pulsed-field ionization spectra. To date, however, these MQDT studies have been limited to a consideration of rotational and electronic effects, and the vibrational dynamics have not been included. Incorporation of the vibrational dynamics into the calculation is expected to be extremely enlightening, particularly with respect to understanding the combined rotational, vibrational, and electronic dynamics associated with Renner-Teller and Jahn-Teller interactions.

More detailed experimental data, both on the spectroscopy and decay dynamics of the autoionizing levels, will also be necessary to provide the most direct

comparison with theory. Very-high-resolution single-photon ionization spectra of NH_3 near the ionization threshold have recently been reported (86), and the extension and analysis of such spectra, particularly in concert with MQDT calculations, will certainly advance current understanding. Recent developments in IR-UV and IR-VUV double-resonance techniques are also expected to simplify the analysis of the spectroscopic data and to provide access to vibrations that are difficult to excite using other methods (54, 87, 88). For example, the IR-UV double-resonance technique has been used to probe Rydberg states of NH_3 in which the ν_3 asymmetric stretch was excited by first pumping the ν_3 fundamental with the IR light and then probing the electronic transition with the UV light (54). Direct excitation of NH_3 Rydberg states with ν_3 excitation is difficult because the Franck-Condon factors for the required transitions are very poor. In NH_3, such techniques will aid in the spectroscopic assignments of the high Rydberg states and make it considerably easier to compare autoionization processes for all four vibrational modes of the molecule. The development of these and other techniques will allow the study of a much broader range of molecules, providing a better assessment of the generality and limitations of current understanding.

Photoelectron spectroscopy using tunable, single-photon ionization with synchrotron or conventional light sources has been used for many years to study the photoionization dynamics of molecules (30, 89, 90). However, even for small polyatomic molecules, the wavelength resolution of this approach has generally been insufficient to resolve the rotational structure of the autoionizing resonances, and the assignment of the spectra is difficult. Furthermore, single-photon techniques limit the selectivity of the excitation process and only allow the study of resonances with reasonable Franck-Condon factors to the ground state. One valuable aspect of the approach, however, has been the determination of wavelength-dependent photoelectron angular distributions over extended regions of the spectrum (89–91). These angular distributions can provide detailed information about the partial wave composition of the ejected photoelectron. When coupled with the rotational resolution and selectivity of the laser-based approaches discussed here, these angular distributions can be extremely valuable. Perhaps the most direct approach for recording such angular distributions is to use photoelectron imaging techniques (92, 93). Many of these studies have already been performed on direct photoionization processes, and there is considerable potential for studies on the resonant phenomena discussed here. One example involves the vibrational autoionization of H_3 via the nontotally symmetric vibration, ν_2. In the Jahn-Teller mechanism of Section 5, $\Delta v_2 = -1$ vibrational autoionization occurs with a change in the rotational symmetry, but no change in ℓ of the Rydberg/ejected electron. Although not included in the calculations discussed in Section 5, additional mechanisms for similar processes exist in which ℓ also changes. In principle, photoelectron angular distributions could allow the determination of the relative importance of the two mechanisms.

Finally, this discussion has only concerned vibrational autoionization processes. In general, the dissociation energies of most molecules lie below their ionization

potentials. Thus, the autoionizing resonances may also predissociate to neutral fragments, as discussed above in the context of dissociative recombination. Generally, the interaction between dissociation and ionization phenomena can result in very interesting dynamics, as in the case of NO (94). Studies of the neutral dissociation dynamics will complement the studies on the ionization dynamics, and ultimately provide a much better picture of the dynamics of highly energized Rydberg states.

In conclusion, recent experimental and theoretical advances have created an exciting opportunity for making considerable progress in our understanding of molecular photoionization dynamics and, more generally, in our understanding of the interactions among the rotational, vibrational, and electronic degrees of freedom in isolated, highly energized molecules.

ACKNOWLEDGMENTS

I would like to thank J.A. Bacon, C.A. Raptis, P. Bell, F. Aguirre, E.R. Grant, and C. Jungen for helpful conversations and for their contributions to the work reported here. I would also like to thank H. Helm for the permission to use Figures 8 and 10, and R.A. Gangi for permission to use Figure 7. This work was supported by the U.S. Department of Energy, Office of Science, Office of Basic Energy Sciences, Division of Chemical Sciences, Geosciences, and Biological Sciences, under Contract W-31–109-Eng-38.

LITERATURE CITED

1. Mulliken RS. 1928. *Phys. Rev.* 32:186–222
2. Mulliken RS. 1932. *Rev. Mod. Phys.* 4:1–86
3. Walsh AD. 1953. *J. Chem. Soc.* 1953: 2260–330
4. Buenker RJ, Peyerimhoff SD. 1974. *Chem. Rev.* 74:127–88
5. Jean Y, Volotran F, Burdett JK. 1993. *An Introduction to Molecular Orbitals*. New York: Oxford Univ. Press. Edited and translated by Jeremy Burdett, Copyright 1993 by Oxford University Press, Inc.
6. Lowry TH, Schueller Richardson K. 1976. *Mechanism and Theory in Organic Chemistry*. New York: Harper & Row
7. Burdett JK. 1980. *Molecular Shapes*. New York: Wiley
8. Berry RS. 1966. *J. Chem. Phys.* 45:1228–45
9. Field RW. 1981. *Disc. Faraday Soc.* 71: 111–23
10. Field RW. 1987. *J. Phys. Coll. C* 7:12–28
11. Pratt ST. 1995. *Rep. Prog. Phys.* 58:821–83
12. de Lange CA. 2001. *Adv. Chem. Phys.* 117:1–125
13. Jungen C. 1996. *Molecular Applications of Quantum Defect Theory*. Philadelphia: Inst. Phys.
14. Greene CH, Jungen C. 1985. *Adv. At. Mol. Phys.* 21:51–121
15. Ross S. 1991. In *Half-Collision Resonance Phenomena in Molecules*, ed. M García-Sucre, G Raseev, SC Ross, pp. 73–110. New York: Am. Inst. Phys.

16. Fielding HH. 2005. *Annu. Rev. Phys. Chem*. 56:In press
17. Bardsley JN. 1967. *Chem. Phys. Lett.* 1: 229–32
18. Berry RS, Nielsen SE. 1968. *J. Chem. Phys.* 49:116–21
19. Nielsen SE, Berry RS. 1968. *Chem. Phys. Lett.* 2:503–6
20. Berry RS, Nielsen SE. 1970. *Phys. Rev. A* 1:383–94
21. Dehmer PM, Chupka WA. 1976. *J. Chem. Phys.* 65:2243–73
22. Dehmer PM, Chupka WA. 1977. *J. Chem. Phys.* 66:1972–81
23. Jungen C, Pratt ST, Ross SC. 1995. *J. Phys. Chem.* 99:1700–10
24. Fujii M, Sato K, Kimura K. 1987. *J. Phys. Chem.* 91:6507–10
25. Hager J, Smith MA, Wallace SC. 1985. *J. Chem. Phys.* 83:4820–22

25a. Hager J, Smith MA, Wallace SC. 1986. *J. Chem. Phys.* 84:6771–80

26. Fano U. 1975. *J. Opt. Soc. Am.* 65:979–87
27. Seaton MJ. 1983. *Rep. Prog. Phys.* 46: 167–257
28. Herzberg G, Jungen C. 1972. *J. Mol. Spectrosc.* 41:425–86
29. Jungen C, Pratt ST. 1997. *J. Chem. Phys.* 106:9529–38
30. Berkowitz J. 1979. *Photoabsorption, Photoionization, and Photoelectron Spectroscopy*. New York: Academic
31. Staib A, Domcke W. 1990. *Z. Phys. D* 16:275–82
32. Stephens JA, Greene CH. 1994. *Phys. Rev. Lett.* 72:1624–27
33. Stephens JA, Greene CH. 1995. *J. Chem. Phys.* 102:1579–91
34. Greene CH, Stephens JA. 1997. *Philos. Trans. R. Soc. London Ser. A* 355:1609–21
35. Kokoouline V, Greene CH, Esry BD. 2001. *Nature* 412:891–94
36. Kokoouline V, Greene CH. 2003. *Phys. Rev. Lett.* 90:133201
37. Kokoouline V, Greene CH. 2003. *Phys. Rev. A* 68:012703
38. Ross SC, Jungen C. 1987. *Phys. Rev. Lett.* 59:1297–1300
39. Ross SC, Jungen C. 1994. *Phys. Rev. A* 49:4353–63
40. Ross SC, Jungen C. 1994. *Phys. Rev. A* 50:4618–28
41. Fano U. 1970. *Phys. Rev.* 2:353–65
42. Chang ES, Fano U. 1972. *Phys. Rev. A* 6:173–85
43. Mistrik I, Reichle R, Müller U, Helm H, Jungen M, Stephens JA. 2000. *Phys. Rev. A* 61:033410
44. Petsalakis ID, Theodorakopoulos G, Child MS. 2001. *J. Chem. Phys.* 115: 10394–403
45. Mulliken RS. 1964. *J. Am. Chem. Soc*. 86: 3183–97
46. Mulliken RS. 1966. *J. Am. Chem. Soc*. 88: 1849–61
47. Mulliken RS. 1969. *J. Am. Chem. Soc*. 91: 4615–21
48. Herzberg G. 1950. *Spectra of Diatomic Molecules*. New York: Van Nostrand Reinhold
49. Bacon JA, Pratt ST. 2000. *J. Chem. Phys.* 113:7188–96
50. Miller PJ, Colson SD, Chupka WA. 1988. *Chem. Phys. Lett.* 145:183–87
51. Mahon BH. 1975. *University Chemistry*. Reading, MA: Addison-Wesley
52. Herzberg G. 1966. *Molecular Spectra and Molecular Structure*. Vol. III. *Electronic Spectra and Electronic Structure of Polyatomic Molecules*. New York: Van Nostrand Reinhold
53. Allen JM, Ashfold MNR, Stickland RJ, Western CM. 1991. *Mol. Phys.* 74:49–60
54. Haber KS, Wiedmann RT, Campos FX, Zwanziger JW, Grant ER. 1989. *Chem. Phys.* 129:73–81
55. Campos FX, Jiang Y, Grant ER. 1990. *J. Chem. Phys.* 93:2308–27
56. Campos FX, Jiang Y, Grant ER. 1992. *J. Chem. Phys.* 94:5897–906
57. Bryant GP, Jiang Y, Grant ER. 1992. *J. Chem. Phys.* 96:4827–40
58. Bryant GP, Jiang Y, Martin M, Grant ER. 1994. *J. Chem. Phys.* 101:7199–210

59. Matsui H, Grant ER. 1996. *J. Chem. Phys.* 104:42–47
60. Bell P, Aguirre F, Grant ER, Pratt ST. 2004. *J. Chem. Phys.* 120:2667–76
61. Burnelle L, May AM, Gangi RA. 1968. *J. Chem. Phys.* 49:561–69
62. Jungen C. 1970. *J. Chem. Phys.* 53:4168–82
63. Staib A, Domcke W, Sobolewski AL. 1991. *Chem. Phys. Lett.* 156:21–31
64. Herzberg G. 1979. *J. Chem. Phys.* 70: 4806–7
65. Dabrowski I, Herzberg G. 1980. *Can. J. Phys.* 58:1238–49
66. Herzberg G, Watson JKG. 1980. *Can. J. Phys.* 58:1250–58
67. Gellene GI, Porter RF. 1983. *J. Chem. Phys.* 79:5975–81
68. Figger H, Fukuda Y, Ketterle W, Walther H. 1984. *Can. J. Phys.* 62:1274–79
69. Figger H, Ketterle W, Walther H. 1989. *Z. Phys. D* 13:129–37
70. Ketterle W, Figger H, Walther H. 1989. *Z. Phys. D* 13:139–46
71. Helm H. 1986. *Phys. Rev. Lett.* 56:42–45
72. Dodhy A, Ketterle W, Messmer HP, Walther H. 1988. *Chem. Phys. Lett.* 151: 133–37
73. Lembo LJ, Bordas MC, Helm H. 1990. *Phys. Rev. A* 42:6660–69
74. Bordas MC, Lembo LJ, Helm H. 1991. *Phys. Rev. A* 44:1817–27
75. Reichle R, Mistrik I, Müller U, Helm H. 1999. *Phys. Rev. A* 60:3929–42
76. Bunker PR, Jensen P. 1998. *Molecular Spectroscopy and Molecular Symmetry*. Ottawa: NRC-CNRC. 2nd ed.
77. Longuet-Higgins HC. 1961. *Adv. Spectrosc.* 2:429–72
78. Deleted in proof
79. Pan SH, Lu KT. 1988. *Phys. Rev. A* 37:299–302
80. Staib A, Domcke W. 1993. *Chem. Phys. Lett.* 204:505–10
81. Staib A, Domcke W, Sobolewski AL. 1990. *Z. Phys. D* 16:49–60
82. Child MS, Jungen C. 1990. *J. Chem. Phys.* 93:7756–66
83. Vrakking MJJ, Lee YT, Gilbert RD, Child MS. 1993. *J. Chem. Phys.* 98:1902–15
84. Child MS, Glab WL. 2000. *J. Chem. Phys.* 112:3754–65
85. Dickinson H, Rolland D, Softley TP. 2001. *J. Phys. Chem. A* 105:5590–600
86. Seiler R, Hollenstein U, Softley TP, Merkt F. 2003. *J. Chem. Phys.* 118:10024–33
87. Ebata T, Fujii A, Mikami N. 1998. *Int. Rev. Phys. Chem.* 17:331–61
88. Qian XM, Kung AH, Zhang T, Lau KC, Ng CY. 2003. *Phys. Rev. Lett.* 91:233001
89. Dehmer JL, Parr AC, Southworth SH. 1987. See Ref. 95, pp. 241–353
90. Nenner I, Beswick JA. 1987. See Ref. 95, pp. 355–466
91. Reid KL. 2003. *Annu. Rev. Phys. Chem.* 54:397–424
92. Suits AG, Continetti RE, eds. 2000. *Imaging in Chemical Dynamics*. Washington, DC: Am. Chem. Soc.
93. Whitaker B, ed. 2003. *Imaging in Molecular Dynamics*. New York: Cambridge Univ.
94. Giusti-Suzor A, Jungen C. 1984. *J. Chem. Phys.* 80:986–1000
95. Marr GV, ed. 1987. *Handbook on Synchrotron Radiation*. Amsterdam: North-Holland

Annual Review of Physical Chemistry
Volume 56, 2005

CONTENTS